processes

MDPI

Article

Environmental Cracking Failure Analysis of Stainless Steel Threaded Joint in Rotary Steerable Tool

Yuhong Jiang [1,2], Hualin Zheng [1,*], Jiancheng Luo [3], Ke Zhang [3], Zhengpeng Du [3], Wei Liu [4], Zhiming Yu [5] and Dezhi Zeng [3,*]

[1] School of Mechatronic Engineering, Southwest Petroleum University, Chengdu 610500, China
[2] CNPC Chuanqing Drilling Engineering Co., Ltd., Chuanxi Drilling Company, Chengdu 610500, China
[3] State Key Laboratory of Oil & Gas Reservoir Geology and Exploitation, Southwest Petroleum University, Chengdu 610500, China
[4] Drilling and Production Engineering Technology Research Institute, CNPC Chuanqing Drilling Engineering Co., Ltd., Chengdu 610051, China
[5] Research Institute of Natural Gas Technology, PetroChina Southwest Oil and Gas Field Company, Chengdu 610213, China
* Correspondence: 13709038896@163.com (H.Z.); zengdezhi1980@163.com (D.Z.)

Abstract

Axial cracking in threaded joints of rotary steerable tools is a critical but under-investigated failure mode that can severely disrupt shale gas drilling operations. Understanding its root cause is essential for prevention. This study aims to determine the cause of an axial cracking failure in an S35150 austenitic stainless steel threaded joint from a field operation. A comprehensive analysis was conducted, integrating physicochemical characterization of the failed joint. The stress corrosion behavior of the threaded joint in a simulated corrosive environment was evaluated via four-point bend (FPB) and double cantilever beam (DCB) stress corrosion tests. The results showed that the material exhibited high susceptibility factors: a hardness of 38.5 HRC, a yield-to-tensile ratio near 1, and a P content exceeding the standard. Fracture surface analysis revealed an intergranular morphology with substantial chlorine (0.78%) and sulfur (0.93%) contents, indicative of stress corrosion cracking (SCC). The laboratory tests results demonstrated that the threaded joint had poor crack resistance: the fracture toughness value of the specimen measured by the DCB test was 24.14 MPa·m$^{0.5}$, and all specimens fractured during the FPB.

Keywords: stress corrosion cracking; threaded joint; rotary steerable tool; failure analysis

Check for updates

Academic Editor: Chin-Hyung Lee

Received: 8 January 2026
Revised: 12 February 2026
Accepted: 14 February 2026
Published: 17 February 2026

Copyright: © 2026 by the authors. Licensee MDPI, Basel, Switzerland. This article is an open access article distributed under the terms and conditions of the Creative Commons Attribution (CC BY) license.

1. Introduction

As an unconventional natural gas resource, shale gas is an indispensable and important component of the global energy landscape [1–3]. However, shale gas development, particularly in regions with thin reservoirs and long horizontal sections, heavily relies on advanced directional drilling technologies [4,5]. Rotary steerable systems (RSS) are pivotal in this context for precise wellbore trajectory control [6]. Within these tools, high-strength threaded joints serve as critical connections, yet they constitute potential weak points [7]. They are subjected to a complex spectrum of mechanical loads while simultaneously being exposed to drilling fluids that often contain high concentrations of corrosive ions, such as chlorides [8–11]. This combination of sustained tensile stress and a corrosive environment creates a significant risk for stress corrosion cracking (SCC), a particularly insidious failure mode that can lead to sudden brittle fracture [12].

Under the synergistic effect of stress and corrosive environment, SCC is an extremely dangerous and insidious failure mode of metallic materials [13]. The occurrence of SCC generally does not require obvious general corrosion; instead, it can induce the initiation and propagation of brittle cracks under static tensile stress far below the yield strength of the material, ultimately leading to catastrophic sudden fracture [14]. Although austenitic stainless steel, which is widely used in the petroleum industry, possesses excellent general corrosion resistance and mechanical properties, it is highly susceptible to SCC in specific environments [15]. Classic chloride-induced SCC is one of the primary failure mechanisms of such materials in oxygen-containing chloride environments, and related accidents have been widely reported [16]. Kryzhanivskyi et al. [17] investigated the fracture of a G105 drill pipe and found that the mechanical properties of the steel were generally up to standard, with only a slight decrease in elongation. The root cause of the failure was that non-metallic inclusions in the microstructure promoted crack initiation. Yu et al. [18] investigated a failure case of S135 drill pipes through a series of experimental tests. They concluded that although the physical and chemical properties of the drill pipes met the standard requirements, the damage of the surface coating induced the initiation of cracks from corrosion pits on the inner wall, which eventually led to sudden fracture under applied stress. Liu et al. [19] conducted a failure analysis of aluminum alloy drill pipes and found that although the chemical composition and conventional mechanical properties of the drill pipes met the standard requirements, the discontinuous banded secondary phases and inclusions in the microstructure increased the brittleness sensitivity of the drill pipes in the corrosive medium of the mud environment. Eventually, the environmental medium induced brittle fracture of the drill pipes. Although cracking cases of drilling tools have been extensively studied, current research has primarily focused on drill pipes, while studies on the failure behavior of rotary steering drilling tools remain relatively limited. The only retrieved case is the research conducted by Wang et al. [20], who adopted a variety of test methods and characterization techniques to investigate the corrosion failure of the pressure-resistant cylinder of measurement-while-drilling tools. They found that large-scale non-metallic inclusions in the material significantly enhanced the susceptibility of the material to SCC. Under the synergistic effect of stress and corrosion, cracks initiated at the bottom of pitting corrosion pits and propagated radially, forming a large number of parallel cracks on the surface of the pressure-resistant cylinder. In addition, traditional cracking modes of drill pipes are dominated by transverse fractures, while reports on axial fractures of drill pipes remain scarce. Current research holds that axial cracks in the drill pipe body fall into the category of SCC [21]. Therefore, despite the established nature of failure analysis techniques, a dedicated investigation into the axial SCC failure of RSS threaded joints, particularly under the synergistic action of high-chloride and sulfide-containing environments, remains lacking. This study addresses this gap by: (1) providing the first comprehensive case analysis of axial cracking in an RSS threaded joint; (2) quantitatively evaluating its SCC susceptibility via FPB and DCB tests in a simulated downhole environment; and (3) elucidating the dominant role of chloride-induced SCC exacerbated by high material strength/hardness. The findings offer novel insights for the material selection and operational protection of such critical components.

This study systematically analyzes the causes of axial cracking in the threaded joints of rotary steering tools used in shale gas drilling operations in Southwest China. The cylinder was fabricated from S35150 austenitic stainless steel and subjected to solution heat treatment. The drilling formation mainly contains pyrite, with a formation temperature of 130 °C. Samples were collected from the vicinity of the joint cracks for analysis, including the determination of elemental composition, metallographic structure, and mechanical properties. The cracked section was split open, and scanning electron microscopy coupled

with energy-dispersive X-ray spectroscopy (SEM-EDS) was employed to characterize the fracture morphology and elemental distribution. To verify the analysis results and evaluate the crack resistance of the joint material, four-point bending (FPB) and double cantilever beam (DCB) stress corrosion tests were conducted on the threaded joints in a simulated environment. These methodologies were designed to clarify the causes of corrosion failure in the pressure-resistant cylinder and propose corresponding protection strategies to extend its service life.

2. Materials and Methods

2.1. Physical and Chemical Performance Test

To verify whether the material of the threaded joint meets the standard requirements, samples were taken near the joint cracks. In accordance with GB/T 11170-2008 [22], the chemical composition of the threaded joint was analyzed using an optical emission spectrometer (SPECTRO MAXx07-F, SPECTRO, Kleve, Germany). Samples were extracted separately along the longitudinal and transverse directions from the area adjacent to the substrate of the threaded joint. After grinding with sandpaper and polishing with diamond powder, the samples were etched. Subsequently, the microstructure of the metal was observed using an optical microscope (Zeiss Axio Scope A1, Oberkochen, Germany). Microstructural examination was conducted to identify key features affecting SCC susceptibility, including, for example, the matrix phase and non-metallic inclusions. Meanwhile, the non-metallic inclusions and grain size grade in the steel were inspected and evaluated in accordance with relevant standards. To prepare for the subsequent four-point bending stress corrosion test, the tensile strength of the material was measured. In compliance with ISO 6892-1:2019 [23], tensile tests were performed using a microcomputer-controlled electro-hydraulic servo universal testing machine (MTS SHT4106-G, MTS, Eden Prairie, MA, USA). In accordance with GB/T 230.1-2018 [24], the hardness of the area near the cracks of the threaded joint was tested using a Huayin digital Rockwell hardness tester (200HRC-150, Huayin Testing Instruments, Yantai, China). Following GB/T 229-2020 [25], Charpy impact tests of the material were carried out on a pendulum impact testing machine (Zwick Roell HIT450P, Ulm, Germany). The V-notched specimens used for the impact tests were machined into standard dimensions of 10 mm × 10 mm × 55 mm. The load–displacement curves and impact absorption energy of the material were recorded by the pendulum impact testing machine. All samples for tensile testing, hardness testing, and Charpy impact testing were taken from the vicinity of the failed joint.

2.2. Four-Point Bend Method

The FPB test is a constant-displacement test. The beam specimen is supported on two glass columns, and loads are applied via another two glass columns to subject one surface of the specimen to tension and the opposite surface to compression. The specimens required for the FPB stress corrosion test are easy to machine, and the test results are intuitive. Therefore, this method has been widely applied in many fields such as material screening and performance evaluation [15]. Based on the cracking behavior of threaded joints, this test method refers to standards including GB/T 40403-2021 [26], NACE TM 0316-2023 [27] and ISO 15156-2 [28]. Specimens with dimensions of 108 mm × 12 mm × 3 mm were cut from the threaded joint by wire electrical discharge machining. Subsequently, the specimens were ground using a metallographic pre-grinder with metallographic sandpapers in the sequence of 280#, 400# and 600#. The purpose of grinding is to obtain a smooth and clean specimen surface and eliminate the residual stress inside the specimens. The stress loading method and the required fixtures used in the test are illustrated in Figure 1. Glass columns were used as insulating materials at the contact positions [29]. To exert 85% of

the actual yield stress on the specimen surface, a certain deflection needs to be applied to the specimens, and the value of this deflection could be calculated using the following Equation (1) [30]:

$$y = \frac{P(3L^2 - 4S^2)}{12Eh} \quad (1)$$

where E is the elastic modulus (253,000 MPa), h is the specimen thickness (3 mm), L and S are the dimensional constants of the four-point bending fixture. Specifically, L refers to the distance between the outer pivot points (100 mm), S refers to the distance between the inner pivot points on the same side (25.6 mm), and P is the stress applied to the specimen surface. After calculation, the deflection value was determined to be 3.552 mm.

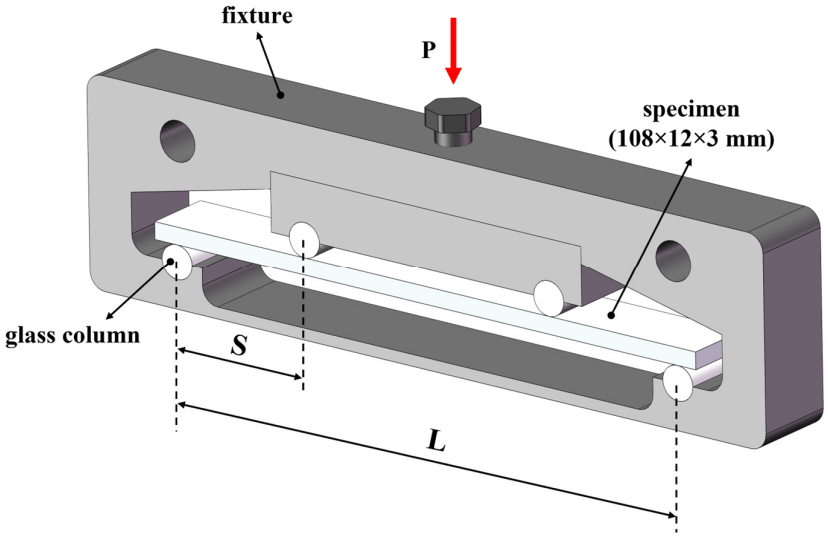

Figure 1. Schematic diagram of FPB Loading.

To simulate the field service conditions, the assembled specimens and fixtures were placed into a high-temperature and high-pressure autoclave fabricated from C-276 nickel-based alloy. Subsequently, a 25% $CaCl_2$ solution with 5% wt field formation cuttings was poured into the autoclave, which was then sealed tightly. After verifying the airtightness, the solution was heated up to 130 °C, and the test duration was set at 720 h. Upon completion of the test, the specimens were detached from the fixtures, followed by cleaning and drying. Then the specimen surface was analyzed using SEM and EDS. The purpose of this experiment was to verify the correctness of the failure analysis.

2.3. Double Cantilever Beam Method

The DCB test is used to measure the resistance of metallic materials to environmentally induced crack propagation, which is characterized by K_{ISCC}, the threshold stress intensity factor for SCC susceptibility, to obtain the rated value of crack growth resistance. The test procedure is independent of the initiation of pits or cracks, as the specimens are pre-cracked prior to testing, and is also independent of the occurrence of failure or non-failure [31].

To further evaluate the SCC susceptibility of the joint material, specimens required for the DCB test were prepared in accordance with standards including NACE TM0177-2016 [32] and GB/T 15970.6-2007 [33] (Figure 2), and the corresponding tests were carried out. The test procedure is illustrated in Figure 3. The specimens were loaded using wedge blocks, and the displacement of the cantilever beams was measured. Subsequently, the specimens were cleaned with petroleum ether and anhydrous ethanol sequentially to remove surface oil stains and water residues. After that, the specimens were placed into a high-temperature and high-pressure autoclave, followed by the addition of 25% $CaCl_2$ solution with 5% wt field formation cuttings. The autoclave was sealed tightly and then heated up to 130 °C.

After 14 days of immersion, the specimens were taken out, and the corrosion products on the surface were cleaned with distilled water, followed by air-blowing to dry the specimen surface. To minimize the influence caused by certain uncertain factors, the retrieved specimens were baked in an oven at 150 °C to remove the hydrogen dissolved in the metal matrix. The dried specimens were subjected to tensile testing on a tensile testing machine to obtain the load–displacement curves. The final equilibrium wedge lift-off load was calculated from the abrupt change point of the slope in the curves [34]. Finally, the crack length was measured using a scale, and the K_{ISCC} value of the joint material was calculated by the following Equation (2) [34,35]:

$$K_{ISCC} = \frac{p \cdot a\left(2\sqrt{3} + 2.38h/a\right)(B/B_n)^{1/\sqrt{3}}}{Bh^{1.5}} \quad (2)$$

where the variable p is the final equilibrium wedge lift off load calculated from an abrupt change in the slope of load–displacement curve, a is the crack length, h is the height of each arm, and B and B_n are the DCB specimen thickness and web thickness, respectively. Three DCB specimens were tested for joint material, and the average is reported here.

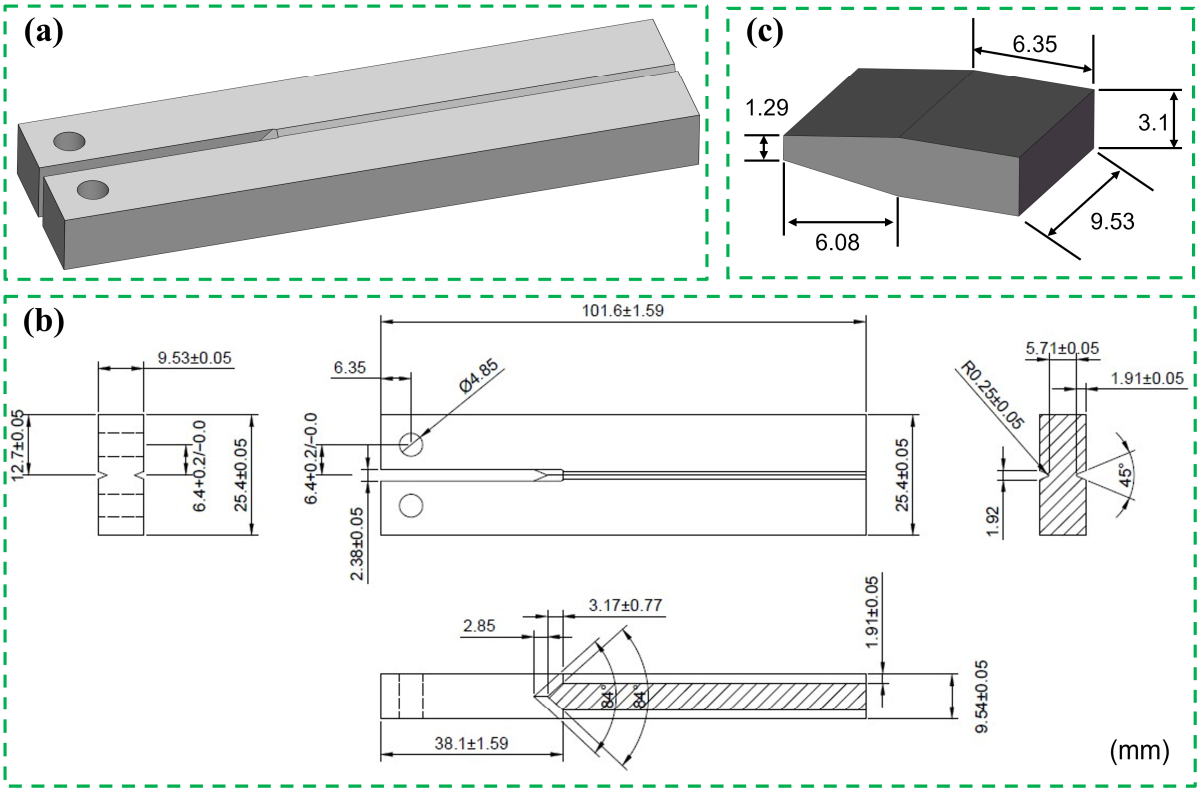

Figure 2. Specimen dimensions and wedges used in the DCB test. (**a**) Geometry of the DCB specimen, (**b**) Dimensions of the DCB specimen, (**c**) Geometry and dimensions of the loading wedge.

2.4. Microscopic Corrosion Morphology Characterization

The cracking surfaces of the fractured joints were examined using scanning electron microscopy (SEM, Model JSM-7500F, Hitachi, Tokyo, Japan) equipped with an energy-dispersive spectrometry (EDS) instrument (Model INCA X-max50, Oxford Instruments, Oxford, UK). This was performed to identify the fracture modes, while simultaneously observing the micromorphology of the corrosion products on the fracture surfaces and analyzing their elemental compositions.

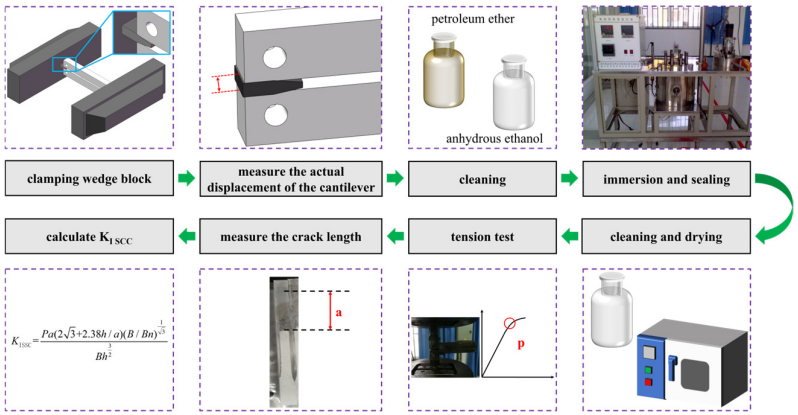

Figure 3. DCB test procedure.

3. Results

3.1. Macroscopic Observation and Media Environment Analysis

The macroscopic examination of the cracked threaded joint was carried out. As shown in Figure 4, at the end of the threaded joint, the crack initiated from the end face and propagated axially along the wall surface. The crack featured a narrow width with a longitudinal propagation length of 108.3 mm, which had radially penetrated the whole wall of joint. Visual inspection revealed no obvious abnormalities in other parts of the threaded joint except for this crack; the internal thread remained bright and clean, and only slight operational marks were observed on the external wall surface. Evidently, this crack was the primary cause of the severe failure of the threaded joint.

Figure 4. Macrograph of the cracked threaded joint.

To analyze the cracking cause of the threaded joint, an investigation was conducted on its service environment. The threaded joint is a component of the rotary steerable drilling tool and was in service during the drilling of a shale gas well in Southwest China. Field data show that the formation where the shale gas is located mainly contains pyrite, with a formation temperature ranging from 130 to 150 °C. The drilling fluid adopted for well drilling is an oxygen-untreated oil-based drilling fluid containing 25% $CaCl_2$.

3.2. Physical and Chemical Tests

Table 1 presents the chemical composition test results of the cracked joint. Compared with the API standard [36], the P content of the threaded joint significantly exceeds the specified limit. Generally, both P and S in austenitic stainless steel can markedly increase its

susceptibility to SCC [37,38]. According to the literature [37,38], phosphorus in austenitic stainless steels tends to segregate to grain boundaries at elevated temperatures, which significantly reduces the grain boundary cohesive energy and makes grain boundaries the preferential path for brittle fracture under the synergistic action of stress and corrosive media. In the present study, the joint was serviced at approximately 130 °C for a long term, which provided favorable conditions for the thermodynamic segregation of phosphorus. Therefore, the non-compliance of the material's elemental composition may be a potential cause of the failure.

Table 1. Chemical composition of the cracked threaded joint (wt.%).

	Element												
	C	**P**	**S**	**Si**	**Ni**	**Cr**	**Mo**	**Al**	**Mn**	**Cu**	**V**	**Ti**	**Fe**
Content	0.06	0.03	0.015	0.20	1.84	17.5	0.10	0.02	14.4	0.16	0.14	0.002	Bal.
API Spec 7-1	-	≤0.02	≤0.015	-	-	-	-	-	-	-	-	-	-

Figures 5 and 6 show the transverse and longitudinal metallographic structures of the fractured threaded joint, respectively. Granular carbides are distributed across the matrix. The spherical pearlite, massive white phases, and granular phases correspond to eutectic carbides and secondary carbides. The microstructure is composed of austenite, massive carbides, and newly formed eutectic ledeburite generated after remelting. Table 2 presents the rating results of non-metallic inclusions, microstructure, and grain size of the joint. The non-metallic inclusions in the joint are categorized as oxide-type D1.0, and the grain size grade is 4.0. The metallographic structure is austenite, which featured relatively coarse grains and incomplete structural transformation.

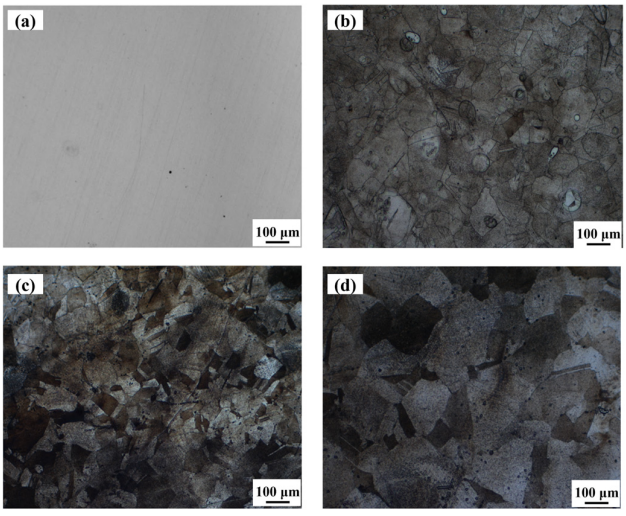

Figure 5. Transverse non-metallic inclusions (**a**), grain size (**b**), and metallographic structure (**c**,**d**).

Table 2. Analysis results of non-metallic inclusions, structure and grain size of the cracked threaded joint.

Sample	**Non-Metallic Inclusions**										**Metallographic Structure**	**Grain Size (Grade)**
	A		**B**		**C**		**D**		**DS**			
	Thin	**Thick**	**Thin**	**Thick**	**Thin**	**Thick**	**Thin**	**Thick**	**Thin**	**Thick**		
Horizontal	-	-	-	-	-	-	-	1.0	-	-	Austenite	4.0
Vertical	-	-	-	-	-	-	1.0	-	-	-	Austenite	4.0

Note: A refers to sulfide-type inclusions, B refers to alumina-type inclusions, C refers to silicate-type inclusions, D refers to circular oxide-type inclusions, and DS refers to single-particle spherical-type inclusions.

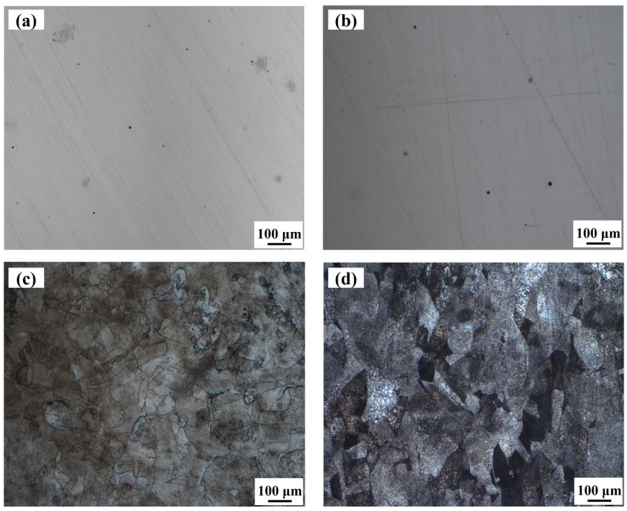

Figure 6. Longitudinal non-metallic inclusions (**a**), grain size (**b**), and metallographic structure (**c**,**d**).

The mechanical property test results of the joint are shown in Table 3. It is evident that all mechanical properties meet the requirements specified in the API standard. Specifically, the steel grade of the joint reaches 160 ksi. Meanwhile, the ratio of tensile strength to yield strength is close to 1, resulting in an extremely limited deformation capacity of the material prior to fracture. Studies have indicated that a higher ratio of tensile strength to yield strength is detrimental to the damage resistance of materials under load-bearing conditions [39]. Therefore, high strength and hardness are concluded to have significantly heightened the material's susceptibility to cracking under the synergistic action of stress and corrosion. In particular, during the drilling process, the joint, as a connecting component between the front and rear sections, sustains complex loading, which may lead to premature failure. The study concludes that the lower the hardness of a material, the better its resistance to SCC [21,40]. For instance, steel materials with a hardness below 22 HRC generally have a low probability of suffering from SCC [41,42]. However, in this case, the surface hardness of the joint reached 38.5 HRC, which is significantly higher than 22 HRC.

Table 3. Results of the mechanical property test.

Test Result	Yield Strength (MPa)	Tensile Strength (MPa)	Elongation After Fracture (%)	Impact Test Result KV2 (J)	Hardness (HRC)
Test value	1159	1163	18.2	216.59	38.5

Therefore, comprehensive physical and chemical performance tests reveal that both the excessive elemental compositions and the mechanical properties of high strength and high hardness have increased the cracking susceptibility of the joint.

3.3. Observation of Crack

To analyze the micro-characteristics of the cracking position of the threaded joint under actual service conditions, a sample containing the end of the longitudinal crack was cut from the threaded joint, as shown in Figure 7a, and then split along the crack. The macroscopic morphology of the fracture surface after splitting the crack is presented in Figure 7b, which shows distinct color zoning. The upper part belongs to the aged fracture surface, which was generated in the service environment. Therefore, this part of the fracture surface was eroded by corrosive media in the service environment, resulting in a black-brown color. The lower part is the fresh fracture surface, where the metal substrate was oxidized upon exposure to air, showing a metallic gray color. As can be seen from

Figure 7b, the crack propagated from the port of the threaded joint toward the pipe body. A preliminary observation of the split fracture surface was conducted using SEM. As shown in Figure 7c, the fracture surface was generally flat without obvious plastic deformation. A significant difference was observed between the old fracture zone and the fresh fracture zone: the fresh fracture zone was cleaner and free of the flocculent substances attached to the old fracture zone.

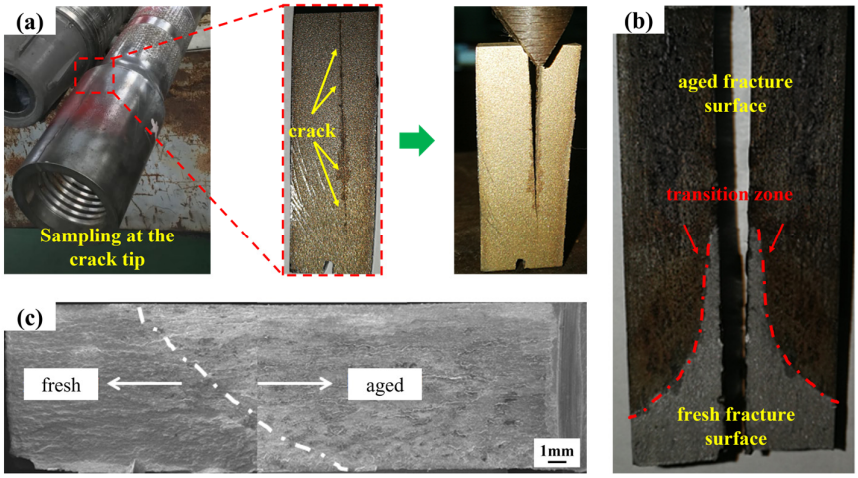

Figure 7. Crack fracture surface analysis process: (**a**) after sampling at the crack tip, the sample was split along the crack; (**b**) macroscopic fracture morphology image; (**c**) microscopic fracture morphology image.

The aged fracture surface, including the corroded area and microcracks, was observed in detail by SEM, as shown in Figure 8. Figure 8a1–a3 display the corroded area, which exhibits disordered protrusions. Upon local magnification, a large number of spherical particles with varying sizes can be observed. Figure 8b1–b3 show the microcrack area, where the cracks are of different lengths and mostly arc-shaped. Obvious crack opening was observed, exhibiting the characteristics of stress-induced crack propagation. It is proposed that the region with the widest crack width corresponds to the crack initiation site [15]. As shown in Figure 8a2, signs of corrosion are also present in the crack region. The results of the EDS analysis on both the corroded area and the cracked area indicate that the elements with relatively high contents on the aged fracture surface mainly include C, Fe, O, Ca, S, and Cl. This implies that the corrosion products are primarily composed of oxygen corrosion products and scale deposits, where Ca, S, and Cl are all derived from the service environment of the joint. The formation of cracks provides channels for the infiltration of these ions, accelerating their contact with the crack surfaces of the joint. The contents of chlorine and sulfur elements are as high as 0.78% and 0.93%, respectively. Among these ions, chloride ions feature a small atomic radius and strong penetrability, which can easily induce SCC of the material [43,44].

The SEM images of the transition zone and the fresh fracture surface are shown in Figure 9. It can be seen from Figure 9a1,a2 that there are some small dimples and fishbone patterns in the transition zone. In addition, a white tear ridge can be observed in the upper right corner. Obviously, the crack propagation direction and fracture characteristics of the transition zone correspond to quasi-cleavage fracture. Figure 9b1,b2 present the SEM images of the fresh fracture surface. The entire fracture surface exhibits a large area of river patterns, with clustered small dimples in local regions. This indicates that the fresh fracture surface of the specimen is a typical quasi-cleavage brittle fracture under the action of an external splitting force.

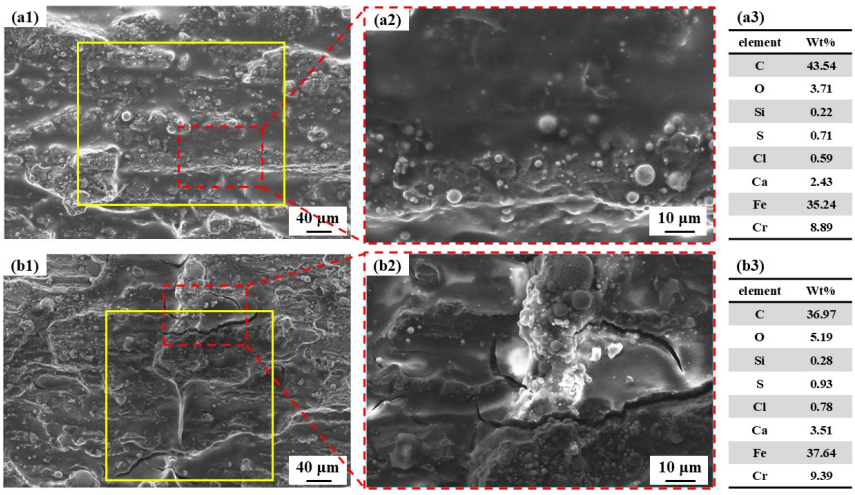

Figure 8. SEM morphology of the aged fracture surface and EDS analysis of the selected area: (**a1**) SEM image of the corroded area; (**a2**) magnified image of red box in (**a1**); (**a3**) elemental content of the yellow selected area in (**a1**); (**b1**) SEM image of the microcrack area; (**b2**) magnified image of red box in (**b1**); (**b3**) elemental content of the yellow selected area in (**b1**).

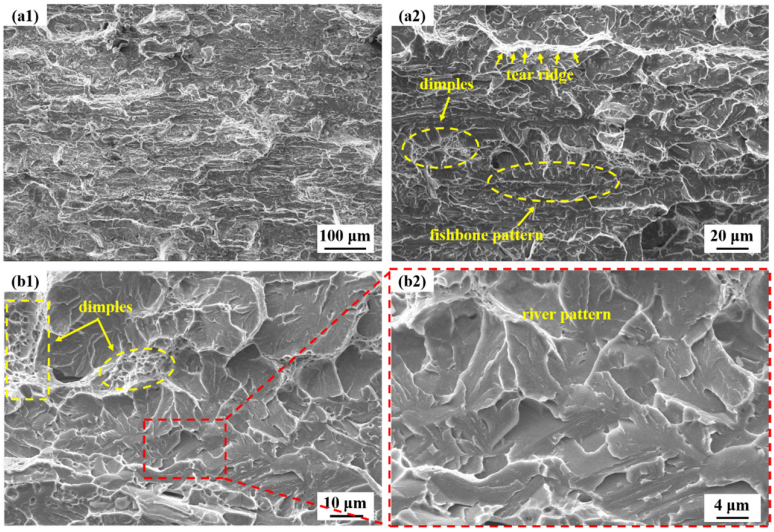

Figure 9. SEM morphology of the transition zone and fresh fracture surface: (**a1**,**a2**) transition zone; (**b1**,**b2**) fresh fracture surface.

To eliminate the interference of corrosion products, the split crack surfaces were cleaned with a freshly prepared film-removing solution (500 mL HCl + 500 mL H_2O + 3.5 g $C_6H_{12}N_4$) at room temperature. Subsequently, the samples were thoroughly rinsed with flowing deionized water for at least 3 min, followed by ultrasonic cleaning in analytical-grade acetone for 5 min to displace residual water. Finally, the samples were dried with a gentle stream of warm nitrogen. After the cleaning process, the aged fracture surface and transition zone were characterized and analyzed by SEM. The fracture morphologies under low magnification are presented in Figure 10a, which shows that the flocculent attachments on the aged fracture surfaces were removed in comparison with the images obtained before cleaning. The images of the aged fracture surface after cleaning are shown in Figure 10b1,b2. It can be observed that there are numerous secondary cracks located at the triple junctions of grain boundaries. The cracks propagate along the grain boundary network, exhibiting polyhedral and rock candy-like boundaries, which is characteristic of typical intergranular brittle fracture. Based on the above findings, the failure mode of the

threaded joint is consistent with that of SCC. SCC is a cracking behavior jointly influenced by stress and corrosion.

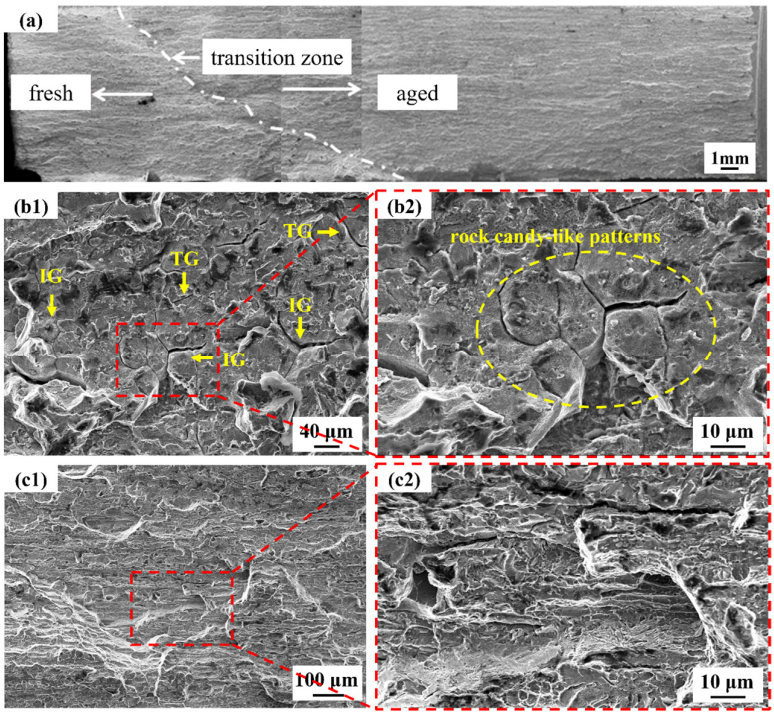

Figure 10. SEM morphologies of the fracture surfaces after cleaning: (**a**) fracture morphologies under low magnification; (**b1**,**b2**) SEM morphologies of the aged fracture surfaces after cleaning; (**c1**,**c2**) SEM morphologies of the transition zone after cleaning.

3.4. Stress Analysis

The failed joint in this case is a female threaded joint, which is a component of the rotary steerable tool. After the joint is manufactured and assembled, it is subjected to considerable tangential tensile stress. This stress varies with the make-up torque of the joint: as the make-up torque increases, the tangential tensile stress rises accordingly. Once cracks initiate, the tangential tensile stress will still promote the further propagation of the cracks. Furthermore, the presence of chlorine and sulfur elements in the service environment exacerbates the SCC of the threaded joints.

3.5. Confirmatory Experiment Result Analysis

From the comprehensive analysis above, we concluded that SCC occurred in the threaded joint caused by Cl^- and stress. To verify the validity of the failure analysis, verification tests were conducted on the threaded joint in the experiments described in Sections 2.2 and 2.3.

After the four-point bending test, the specimens were observed. Figure 11a shows the macroscopic images of the specimens: all three parallel specimens underwent vertical fracture, with the fracture locations close to one end. Due to long-term immersion, the metallic luster of the specimens decreased significantly. There were black deposits on local areas of the specimen surfaces, especially in the contact regions between the specimens and the glass columns. In addition, visible cracks were observed on the specimen surfaces, and the crack propagation direction was consistent with the fracture direction. It is evident that the joint material exhibits poor cracking resistance in the simulated environment and is susceptible to chloride-ion-induced SCC.

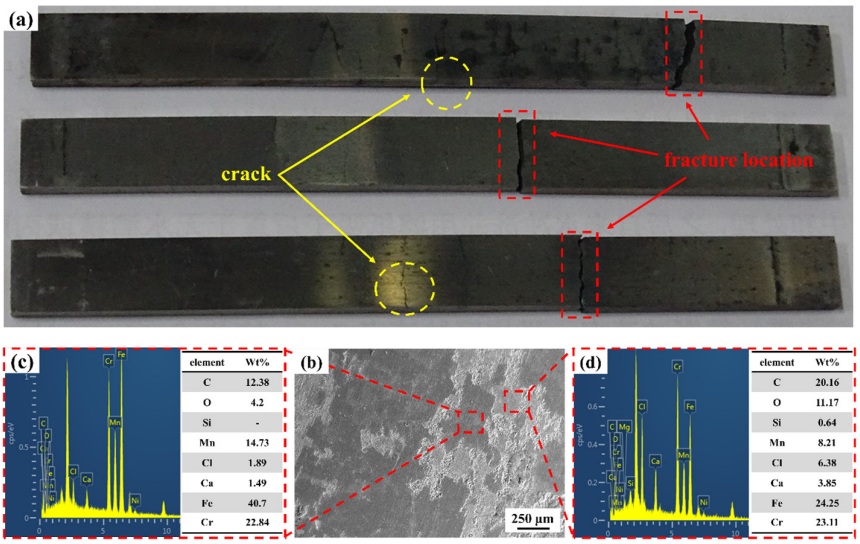

Figure 11. Morphologies of the specimens after four-point bending test: (**a**) macroscopic morphology; (**b**) SEM morphology; (**c**,**d**) element contents in the selected areas of (**b**).

One fractured specimen was selected for surface micromorphology observation and element distribution measurement, with the results presented in Figure 11c,d. As shown in Figure 11b, the darker-colored areas are relatively clean and flat. The EDS results (Figure 11c) indicate a high Fe content of up to 40.7% along with a low O content, suggesting that these areas may be the exposed metal substrate after the detachment of the surface corrosion product film. By contrast, the lighter-colored areas in Figure 11b are rough and covered with deposits, which are likely the regions covered by the corrosion product film. The EDS results (Figure 11d) show that compared with the flat areas, the contents of C, O, Cl and Ca increase significantly, while the contents of matrix elements such as Fe and Mn decrease. This demonstrates that the corrosion product film is mainly composed of oxygen corrosion products and scale deposits, which is consistent with the element detection results of the joint fracture surface. In addition, the corrosion products contain a substantial amount of chlorine, with its content increasing from 1.89% to 6.38%.

After the DCB test, the specimens were cleaned and dried. Due to the difficulty in clearly observing the cracking status of the specimens upon removal, the crack length could not be determined. Therefore, liquid nitrogen was used to condense the specimens, followed by quench splitting for observation. The cracking status of the specimens can be clearly observed from the photos of the specimens split after liquid nitrogen quenching (Figure 12). There was a distinct boundary between the crack at arrest and the fresh fracture surface formed by quench splitting of the material, and the accurate crack length (a) could be obtained through measurement. All parameters measured in the test and the calculated KI SCC results are presented in Table 4. The crack length (a) of the joint ranges from 36.91 mm to 37.04 mm, and the average K_{ISCC} value of the joint material is 24.14 MPa·$m^{0.5}$. Currently, there are no standards that directly specify the fracture toughness values of drilling tools. Even the GB/T 20972.3-2025 [45] states that the acceptance criteria for fracture toughness tests should be determined by the user. Considering that tubing, casing, and drilling tools are both downhole strings, the limits on the fracture toughness of casing and tubing specified in GB/T 19830-2023 [46] were referenced. According to this standard, the minimum fracture toughness values determined via the DCB test are 33.0 MPa·$m^{0.5}$ for C90 and T95 grade steel specimens, and 26.4 MPa·$m^{0.5}$ for C110 grade steel specimens. Although direct comparison cannot be made due to the differences in specific service environments and applied loads, it can still be concluded that the fracture toughness of the joint material is relatively poor, which consequently led to the axial cracking of the

joint. This conclusion is also corroborated by the results of the four-point bending tests. This result indicates that for critical components such as rotary steerable tools operating in highly corrosive and high-stress environments, material specifications should mandatorily incorporate the fracture toughness (K_{ISCC}) measured in simulated service environments, and use it as the basis for damage-tolerance design and the determination of non-destructive testing intervals. Current material selection criteria based on room-temperature mechanical properties must be supplemented by environmental fracture resistance evaluations to avoid such cracking.

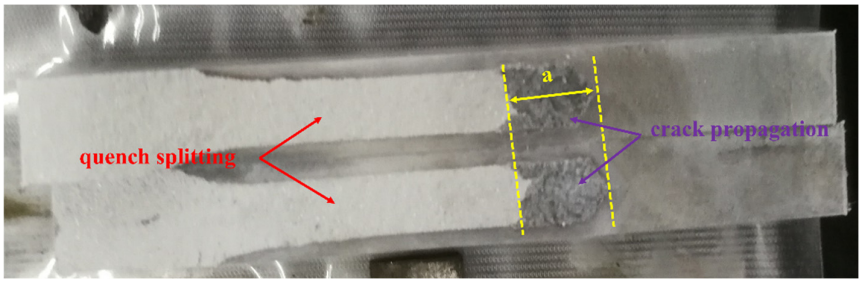

Figure 12. Macroscopic morphologies of specimens split after rapid cooling in liquid nitrogen.

Table 4. Test results of joint fracture toughness K_{ISCC} (MPa·m$^{0.5}$).

Number	a/mm	D/mm	d/mm	h/mm	B/mm	B_n/mm	K_{ISCC}	
							Measured Value	Average Value
1	37.02	17.50	17.95	12.28	9.50	6.16	25.34	24.14
2	37.04	17.47	17.92	12.31	9.49	6.21	22.23	
3	36.91	17.50	17.92	12.30	9.50	6.11	24.84	

As can be seen from Figure 13, the crack propagated gradually from the inverted V-shaped region to the other end during immersion. Owing to the contact between the corrosive medium and the fracture surface, the fracture exhibited a black-gray appearance and was thus referred to as an aged fracture surface. After immersion, the fracture surface formed by quenching and splitting showed an off-white color because the metal matrix was exposed to air, and it was defined as a fresh fracture surface.

Figure 13a,b show the magnified images of the aged fracture surface in the inverted V-shaped region and the transition region between the aged fracture surface and the fresh fracture surface, respectively. The aged fracture surface exhibits a rugged and undulating morphology, while the fresh fracture surface is relatively flat with numerous facets. Magnified observation of the fresh fracture surface (Figure 13c1) reveals that it is mainly composed of flat planes with varying sizes. Further magnification of one of the larger planes (Figure 13c2) shows distinct river patterns, indicating that the fresh fracture is a cleavage fracture. Elemental analysis was performed on the area enclosed by the yellow box in Figure 13c1, and the results show that the main elements include C, Cr, Mn, Fe and Ni, which are basically consistent with the elements of the metal matrix. Magnified observation of the aged fracture surface (Figure 13d1) shows an uneven surface with some particles and microcracks. Further magnification of the central area (Figure 13d2) reveals a mixed morphology, including small flat fracture facets and multiple cracks along the grain boundaries; this morphology is generally regarded as intergranular fracture (IG) [34]. In addition, the presence of tear ridges and steps indicates the occurrence of transgranular fracture (TG) [34]. Elemental analysis was carried out on the area marked by the yellow box in Figure 13d1, and the results demonstrate the presence of S and Cl with contents of 1.41% and 0.85%, respectively, in addition to the matrix metal elements and C. S and Cl

are derived from the solution medium, indicating that corrosive ions penetrated into the cracks and came into contact with the fracture surface during the immersion period.

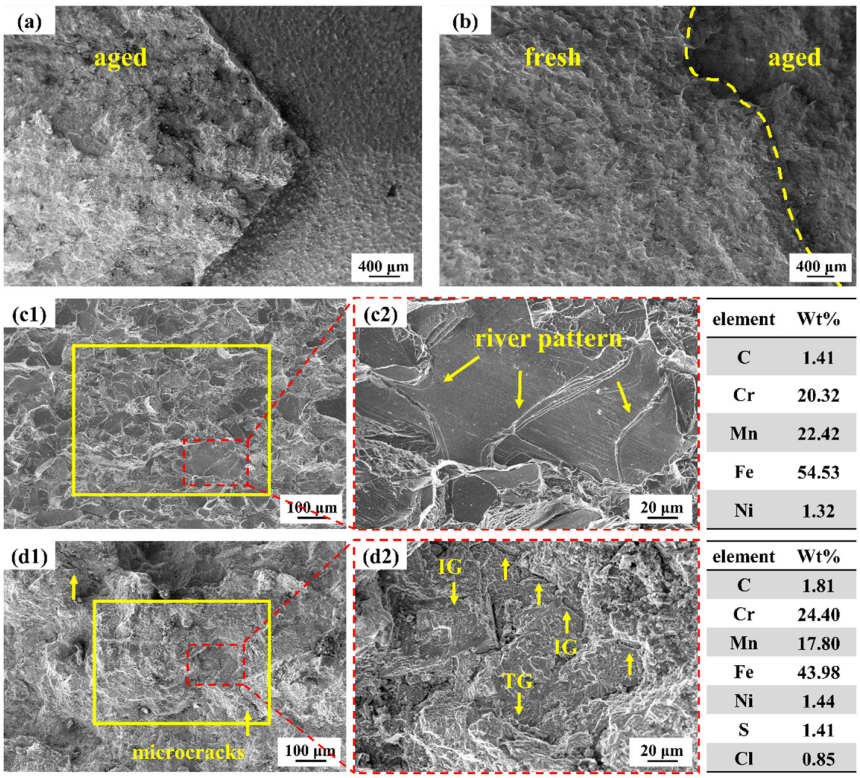

Figure 13. The fractographic features of DCB tested specimen: (**a**) morphology of the crack tip region; (**b**) transition region between the aged fracture surface and the fresh fracture surface; (**c1**) magnified image of the fresh fracture surface; (**c2**) locally magnified image of the red box in (**c1**); (**d1**) magnified image of the aged fracture surface; (**d2**) locally magnified image of the red box in (**d1**).

4. Failure Mechanism Analysis

Cracking is a common failure mode of oil tubular strings. However, as stated in the introduction, most of the currently studied fractures are related to the transverse fractures of tubular strings, while reports on the axial fractures of joints remain scarce. In this case, the fracture surface of the threaded joint showed no obvious characteristics of plastic deformation. A large number of secondary cracks existed at the triple junctions of grain boundaries, presenting a distinct rock-candy-like morphology, which is typical of intergranular brittle fracture. According to the EDS analysis results, the contents of chlorine and sulfur in the corrosion products on the fracture surface were 0.78 and 0.93, respectively. The fracture of the threaded joint was SCC occurring in a sulfide-bearing chloride environment, with chloride ions as the dominant corrosive species.

It is generally accepted that the occurrence of SCC requires a specific combination of three essential factors, namely considerable tensile stress, a specific corrosive environment and a susceptible material [47]. Therefore, the failure mechanism is discussed from these three aspects below.

In this case, as a component of the rotary steering tool, the threaded joint is subjected to dynamic stress during service. More importantly, the special structure of the thread subjects the joint to considerable tangential tensile stress [48]. To establish a complete mechanical-environmental coupled failure mechanism, the tangential tensile stress induced by make-up torque is quantitatively analyzed using a simplified analytical model. The 4 1/2 REG is an API standard rotary-shouldered thread, whose geometric parameters are listed in Table 5.

Table 5. Geometric and mechanical parameters of 4 1/2 REG female thread.

Parameter	Value
Pitch (p)	5.08 mm
Pitch diameter (d_2)	114.3 mm
Inner radius of female thread (r_1)	50.8 mm
Outer radius of female thread (r_2)	63.5 mm
Thread engagement length (L)	63.5 mm
Makeup torque (T)	24,400 N·m
Friction coefficient (μ)	0.12
Stress concentration factor (K_t)	1.37 [49]

The relationship between make-up torque and axial preload is given by:

$$T = F \cdot \frac{d_2}{2} \cdot \tan(\lambda + \rho) \tag{3}$$

where λ is the helix angle and ρ = arctan (μ) is the friction angle.

The equivalent internal pressure on the thread engagement surface is derived from axial preload:

$$p = \frac{F}{\pi d_2 L} \tag{4}$$

The tangential stress at the inner wall of the female thread is calculated using Lame's equation [50]:

$$\sigma_\theta = p \cdot \frac{{r_2}^2 + {r_1}^2}{{r_2}^2 - {r_1}^2} \tag{5}$$

The actual engineering tangential tensile stress is corrected by the stress concentration factor [51]:

$$\sigma_t = K_t \cdot \sigma_\theta \tag{6}$$

Under the makeup torque T = 24,400 N·m, the tangential tensile stress is calculated as:

$$\sigma_t \approx 870 \text{ MPa} \tag{7}$$

For fixed geometry and material parameters, the tangential stress is linearly proportional to makeup torque:

$$\sigma_t = 0.0356T \tag{8}$$

The calculated tangential tensile stress reaches 75% of the material yield strength, which provides the critical tensile stress required for SCC initiation. In addition, improper operation during the tightening and assembly of the joint may leave gripper bite marks on the outer surface of the joint, and these bite marks tend to induce residual stress [40].

Based on the medium environment analysis in Section 3.1, the formation is dominated by pyrite with a formation temperature of approximately 130 °C. The study holds that pyrite reacts with hydroxide ions at high temperatures, and sulfur enters the solution in the forms of S^{2-} and SO_4^{2-} [52]. Therefore, the drilling fluid absorbs sulfides during its cyclic flow in the drilling process. This explains why a 0.93% sulfur content is detected in the crack fracture of the joint. In addition, the drilling fluid itself contains 25% $CaCl_2$, with the chloride ion concentration reaching 196,400 mg/L. The accelerating effect of high-concentration chloride ions on SCC has been widely reported [53,54].

According to the physicochemical property tests, the joint is a material with high strength and high hardness, featuring a tensile strength of 1163 MPa, a yield strength of 1159 MPa and a surface hardness of 38.5 HRC. Studies have shown that yield strength is a crucial factor affecting the SCC resistance of metallic materials [21,55]. The higher

the strength and hardness of a material, the greater its susceptibility to SCC [21,40]. In addition, the P content in the joint exceeds the standard limit. An increase in P content can enhance the SCC susceptibility of the material [38]. An excessive phosphorus content (0.03 wt.%) constitutes a critical intrinsic material defect. Its origin can be traced back to inadequate process control during steelmaking, which resulted in a residual phosphorus content exceeding the specification limits. During the long-term service of the joint at approximately 130 °C, phosphorus atoms tend to undergo thermal diffusion and segregation at grain boundaries, which significantly reduces the grain boundary cohesion and creates favorable pathways for intergranular corrosion cracking. It should be emphasized that while excessive phosphorus alone is a definitive factor impairing the material's resistance to SCC, it did not act in isolation in this failure incident. Instead, it, in conjunction with high hardness and a low yield-to-tensile strength ratio, formed the brittle foundation of the material and greatly amplified the SCC process synergistically driven by the aggressive environment and high operational stress. Therefore, an excessive phosphorus content was a key link leading to a sharp increase in failure susceptibility, yet the ultimate occurrence of failure still required the combined driving effect of the environmental factors and stress. Therefore, in terms of mechanical properties and elemental composition, the joint itself exhibited high susceptibility to cracking. This conclusion has been further verified by subsequent four-point bending tests.

In summary, the cracking of the threaded joint is the result of the coupling effect of the load, environment and material. Although the metallographic structure of the threaded joint meets the requirements, the elemental composition and mechanical properties increased its susceptibility to cracking. Consequently, the threaded joint undergoes SCC characterized by intergranular fracture under the combined action of complex stress, sulfides and chloride ions.

5. Measures and Recommendations

The results of this study indicate that the cracking of the threaded joint is caused by the synergistic effect of multiple factors. To prevent the recurrence of similar failures, the following preventive measures are proposed:

(1) Material selection:

Since the high hardness and yield-to-tensile ratio were key factors rendering the joint vulnerable, the foremost recommendation is to review material selection. This includes considering a lower strength grade with higher fracture toughness for critical threaded connections in such environments. For instance, studies have demonstrated that tool joint materials with a yield strength of 120 ksi is susceptible to SCC [40]. Therefore, the yield strength of the joint should be avoided exceeding 120 ksi. Furthermore, maintaining the tool joint hardness within HB 285–HB 310 results in excellent resistance to SCC and favorable mechanical properties. In addition, for critical threaded connections in corrosive environments, specify a minimum fracture toughness (K_{ISCC}) value determined via DCB testing in a simulated service environment.

(2) Compositional control:

Enforce strict phosphorus and sulfur limits ($P \leq 0.02$ wt.%, $S \leq 0.015$ wt.%) in material procurement specifications to minimize intrinsic grain boundary embrittlement.

(3) Surface treatment:

Apply a corrosion-resistant coating or low-stress shot peening on the thread external surfaces to introduce beneficial compressive residual stresses and act as a barrier against chloride/sulfide ingress.

(4) Operational changes:

Set an operational upper limit for chloride ion concentration in the drilling fluid based on laboratory threshold testing that is significantly lower than the 196,400 mg/L encountered. Implement effective sulfide scavengers in the fluid system, especially when drilling through pyrite-rich formations. To avoid introducing unnecessary stress concentrators and excessive assembly stress that can initiate or propagate cracks, standardizing assembly procedures remains crucial.

6. Conclusions

This study presented a comprehensive failure analysis to determine the root cause of an axial cracking incident in a stainless steel threaded joint from a rotary steerable tool, employing a combination of field-sample characterization and laboratory simulation tests. The main conclusions are as follows:

(1) This investigation demonstrates that the axial cracking of the threaded joint resulted from chloride-induced SCC, which was critically enabled by high in-service tensile stresses and significantly exacerbated by the material's high strength/hardness and non-standard P content.
(2) The case highlights that for critical threaded connections in corrosive, high-stress downhole environments, facture toughness and SCC resistance in simulated service environments must be key selection criteria. A moderate reduction in strength/hardness for improved toughness can be a life-saving trade-off.
(3) The case underscores the necessity of controlling both chloride ion concentrations in drilling fluids, and the importance of strictly adhering to recommended make-up torque procedures to avoid excessive assembly stress.
(4) Nevertheless, this study still has certain limitations, including the constant-displacement FPB test that served as a qualitative pass/fail indicator but did not provide crack initiation kinetics. The potential synergistic role of hydrogen embrittlement in this specific chloride-sulfide environment also warrants further dedicated investigation. Based on these findings, future work should focus on: establishing quantitative, environment-specific threshold values for hardness and yield-to-tensile ratio for critical RSS threaded connections and conducting slow strain rate tests or monitoring crack initiation in FPB tests to better quantify SCC initiation susceptibility.

Author Contributions: Writing—original draft, conceptualization, project administration, Y.J.; writing—review & editing, software, resources, H.Z.; validation, investigation, visualization, J.L.; formal analysis, visualization, K.Z.; formal analysis, Z.D.; visualization, W.L.; data curation, Z.Y.; methodology, conceptualization, visualization, D.Z. All authors have read and agreed to the published version of the manuscript.

Funding: This research received no external funding.

Data Availability Statement: Data is unavailable due to privacy restrictions.

Conflicts of Interest: Wei Liu was employed by the Drilling and Production Engineering Technology Research Institute, CNPC Chuanqing Drilling Engineering Co., Ltd. Zhiming Yu was employed by the Research Institute of Natural Gas Technology, PetroChina Southwest Oil and Gas Field Company. The remaining authors declare that the research was conducted in the absence of any commercial or financial relationships that could be construed as a potential conflict of interest.

Nomenclature

API	American Petroleum Institute
DCB	Double Cantilever Beam

EDS	Energy-Dispersive X-ray Spectroscopy
EAC	Environmentally Assisted Cracking
FPB	Four-Point Bend
K_{ISCC}	Threshold Stress Intensity Factor for Stress Corrosion Cracking
RSS	Rotary Steerable System
SCC	Stress Corrosion Cracking
SEM	Scanning Electron Microscopy
UTS	Ultimate Tensile Strength
YS	Yield Strength

References

1. Lindequist, D.; Selent, S. Did Shale Gas Green the U.S. Economy? *Energy Econ.* **2025**, *145*, 108388. [CrossRef]
2. McMahon, T.P.; Larson, T.E.; Zhang, T.; Shuster, M. Geologic Characteristics, Exploration and Production Progress of Shale Oil and Gas in the United States: An Overview. *Pet. Explor. Dev.* **2024**, *51*, 925–948. [CrossRef]
3. Zou, C.; Lin, M.; Ma, F.; Liu, H.; Yang, Z.; Zhang, G.; Yang, Y.; Guan, C.; Liang, Y.; Wang, Y.; et al. Development, Challenges and Strategies of Natural Gas Industry under Carbon Neutral Target in China. *Pet. Explor. Dev.* **2024**, *51*, 476–497. [CrossRef]
4. Geng, H.; Zhang, B.; Xie, Y. Rotary Steerable Drilling Technology: Bottlenecks Breakthroughs and Intelligent Trends in China Shale Gas Development. *Processes* **2025**, *13*, 3471. [CrossRef]
5. Zafarian, H.; Ameri, M.; Vaghasloo, Y.A. Error Reduction of Tracking Planned Trajectory in a Thin Oil Layer Drilling Using Smart Rotary Steerable System. *J. Pet. Sci. Eng.* **2021**, *196*, 107668. [CrossRef]
6. Li, F.; Ma, X.; Tan, Y. Review of the Development of Rotary Steerable Systems. *J. Phys. Conf. Ser.* **2020**, *1617*, 012085. [CrossRef]
7. Yang, J.; Meng, W.; Yao, M.; Gao, D.; Zhou, B.; Xu, Y. Calculation Method of Riser Top Tension in Deep Water Drilling. *Pet. Explor. Dev.* **2015**, *42*, 119–122. [CrossRef]
8. Wada, R.; Kaneko, T.; Ozaki, M.; Inoue, T.; Senga, H. Longitudinal Natural Vibration of Ultra-Long Drill String during Offshore Drilling. *Ocean Eng.* **2018**, *156*, 1–13. [CrossRef]
9. Song, J.; Liu, S.; He, Y.; Jiang, S.; Zhou, S.; Zhu, H. The State-of-the-Art Review on the Drill Pipe Vibration. *Geoenergy Sci. Eng.* **2024**, *243*, 213337. [CrossRef]
10. Lv, S.; Ji, B.; Kang, Y.; Zhang, H.; Qin, T.; Chi, J.; Gong, J.; Yang, X. Cause Analysis on Drill Pipe Bending and Fracture. *Eng. Fail. Anal.* **2010**, *17*, 1483–1489. [CrossRef]
11. Cai, M.; Mao, D.; Li, Y.; He, T.; He, M.; Tan, L. Study on the Expansion Characteristics of Oil-Based Drilling Fluid in HTHP Wellbore. *Pet. Res.* **2025**. [CrossRef]
12. Song, H.X.; Zhang, S.L.; Chen, X.W.; Wyclif, K.; Guo, J.X.; Xiong, R.Y.; Wang, L. Research on the Pollution and Damage Mechanism of Drilling Fluid on Casing during Ultra-Deep Well Drilling Process. *Pet. Sci.* **2025**, *22*, 1234–1251. [CrossRef]
13. Vakili, M.; Koutník, P.; Kohout, J.; Gholami, Z. Analysis, Assessment, and Mitigation of Stress Corrosion Cracking in Austenitic Stainless Steels in the Oil and Gas Sector: A Review. *Surfaces* **2024**, *7*, 589–642. [CrossRef]
14. Serafim, F.M.F.; Alabi, W.O.; Oguocha, I.N.A.; Odeshi, A.G.; Evitts, R.; Gerspacher, R.J.; Ohaeri, E.G. Stress Corrosion Cracking Behavior of Selected Stainless Steels in Saturated Potash Brine Solution at Different Temperatures. *Corros. Sci.* **2021**, *178*, 109025. [CrossRef]
15. Wang, X.; Yang, Z.; Wang, Z.; Shi, Q.; Xu, B.; Zhou, C.; Zhang, L. The Influence of Copper on the Stress Corrosion Cracking of 304 Stainless Steel. *Appl. Surf. Sci.* **2019**, *478*, 492–498. [CrossRef]
16. Roy, R.; Qu, H.J.; Mao, K.S.; Wharry, J.P. Chloride-Induced Stress Corrosion Crack Propagation Mechanisms in Austenitic Stainless Steel Are Mechanically Driven. *Scr. Mater.* **2025**, *262*, 116652. [CrossRef]
17. Kryzhanivskyi, E.; Nykyforchyn, H.; Student, Z.; Krechkovska, H.V.; Chudyk, I.I. Role of Nonmetallic Inclusions in Premature Stress-Corrosion Fractures of Drill Pipes. *Mater. Sci.* **2020**, *55*, 822–830. [CrossRef]
18. Yu, Z.; Zeng, D.; Hu, S.; Zhou, X.; Lu, W.; Luo, J.; Fan, Y.; Meng, K. The Failure Patterns and Analysis Process of Drill Pipes in Oil and Gas Well: A Case Study of Fracture S135 Drill Pipe. *Eng. Fail. Anal.* **2022**, *138*, 106171. [CrossRef]
19. Liu, W.; Li, J.; Zhong, Y.; Shi, T.; Zhang, J.; Li, S. Failure Analysis on Aluminum Alloy Drill Pipe with Pits and Parallel Transverse Cracks. *Eng. Fail. Anal.* **2022**, *131*, 105809. [CrossRef]
20. Wang, Y.; Chen, X.; Chen, W.; Pu, W.; Zeng, J.; Luo, J.; Zhang, H.; Zeng, D. Corrosion Failure Analysis of a Pressure-Resistant Cylinder for Measurement While Drilling Tools in Directional Drilling. *Processes* **2025**, *14*, 45. [CrossRef]
21. Liu, Y.; Lian, Z.; Lin, T.; Shen, Y.; Zhang, Q. A Study on Axial Cracking Failure of Drill Pipe Body. *Eng. Fail. Anal.* **2016**, *59*, 434–443. [CrossRef]
22. *GB/T 11170-2008*; Stainless Steel—Determination of Multi-Element Contents—Spark Discharge Atomic Emission Spectrometric Method (Routine Method). Standards Press of China: Beijing, China, 2008.

23. *ISO 6892-1:2019*; Metallic Materials—Tensile Testing—Part 1: Method of Test at Room Temperature. International Organization for Standardization: Geneva, Switzerland, 2019.
24. *GB/T 230.1-2018*; Metallic Materials—Rockwell Hardness Test—Part 1: Test Method. Standards Press of China: Beijing, China, 2018.
25. *GB/T 229-2020*; Metallic Materials—Charpy Pendulum Impact Test Method. Standards Press of China: Beijing, China, 2020.
26. *GB/T 40403-2021*; Corrosion of Metals and Alloys—Methodology for Determining the Resistance of Metals to Stress Corrosion Cracking Using the Four-Point Bend Method. Standards Press of China: Beijing, China, 2021.
27. *NACE TM 0316-2023*; Four-Point Bend Testing of Materials for Oil and Gas Applications. NACE International: Houston, TX, USA, 2023.
28. *ISO 15156-2:2020*; Petroleum and Natural Gas Industries—Materials for Use in H2S-Containing Environments in Oil and Gas Production—Part 2: Cracking-Resistant Carbon and Low-Alloy Steels, and the Use of Cast Irons. International Organization for Standardization: Geneva, Switzerland, 2020.
29. Zhou, C.; Huang, Q.; Guo, Q.; Zheng, J.; Chen, X.; Zhu, J.; Zhang, L. Sulphide Stress Cracking Behaviour of the Dissimilar Metal Welded Joint of X60 Pipeline Steel and Inconel 625 Alloy. *Corros. Sci.* **2016**, *110*, 242–252. [CrossRef]
30. Ding, J.; Zhang, L.; Li, D.; Lu, M.; Xue, J.; Zhong, W. Corrosion and Stress Corrosion Cracking Behavior of 316L Austenitic Stainless Steel in High H_2S-CO_2-Cl^- Environment. *J. Mater. Sci.* **2013**, *48*, 3708–3715. [CrossRef]
31. Galakhova, A.; Prattes, K.; Mori, G. High-Temperature High-Pressure SCC Testing of Corrosion-Resistant Alloys. *Mater. Corros.* **2021**, *72*, 1831–1842. [CrossRef]
32. *NACE TM 0177-2016*; Laboratory Testing of Metals for Resistance to Sulfide Stress Cracking and Stress Corrosion Cracking in H2S Environments. NACE International: Houston, TX, USA, 2016.
33. *GB/T 15970.6-2007*; Corrosion of Metals and Alloys—Stress Corrosion Testing—Part 6: Preparation and Use of Pre-Cracked Specimens for Tests Under Constant Load or Constant Displacement. Standards Press of China: Beijing, China, 2007.
34. Zhou, G.Y.; Wang, X.T.; Cao, G.H.; Russell, A.M.; Luo, M.; Dong, X.M.; Zhang, Z.H. Effect of Double Tempering Process on Sulfide Stress Cracking Susceptibility in API-5CT-C110 Casing Steel. *Corros. Sci.* **2023**, *219*, 111208. [CrossRef]
35. Wang, Z.; Wang, P.; Zeng, D.; Shi, T.; Deng, W. A Study on the Influential Factors of Stress Corrosion Cracking in C110 Casing Pipe. *Materials* **2022**, *15*, 801. [CrossRef]
36. American Petroleum Institute. *API Spec 7-1; Specification for Rotary Drill Stem Elements*; API Publishing Services: Washington, DC, USA, 2011.
37. Manuel, Q.A.L.; Noé, R.O.J.; Del Rosario, D.A.Y.; Ariadna, A.J.I.; Vicente, G.F.; Icoquih, Z.P. Analysis of the Physicochemical, Mechanical, and Electrochemical Parameters and Their Impact on the Internal and External Scc of Carbon Steel Pipelines. *Materials* **2020**, *13*, 5771. [CrossRef]
38. Mohtadi-Bonab, M.A. Effects of Different Parameters on Initiation and Propagation of Stress Corrosion Cracks in Pipeline Steels: A Review. *Metals* **2019**, *9*, 590. [CrossRef]
39. Xu, A.; Wan, Y.; Li, B.; Yang, X.; Ye, M.; Song, X. Stress Ratio Effect on Fatigue Crack Growth Behavior for Steels Related to Yield-to-Tensile Strength Ratio and Fracture Toughness. *Theor. Appl. Fract. Mech.* **2025**, *139*, 105015. [CrossRef]
40. Wang, X.; Li, F.; Liu, Y.; Feng, Y.; Zhu, L. A Comprehensive Analysis on the Longitudinal Fracture in the Tool Joints of Drill Pipes. *Eng. Fail. Anal.* **2017**, *79*, 1–7. [CrossRef]
41. Souza, S.M.C.; Cavalcanti, E.H.D.S.; Abud, I.C.; Centeno, R.O.; Alves, M.R.; Zamora, C.A. Failure Analysis in Heavy-Weight Drillpipes during Drilling Operation of off-Shore Oil Well. In Proceedings of the NACE-International Corrosion Conference Series, San Diego, CA, USA, 16–20 March 2003.
42. Villalba, R.; Díaz, Y.; Peñalver, J.R. Bad Practices in Drilling Operation Promoting Corrosion Failures under High Stress. In Proceedings of the NACE-International Corrosion Conference Series, Houston, TX, USA, 3–7 April 2005. Volume 2005-April.
43. Zhang, N.; Zeng, D.; Xiao, G.; Shang, J.; Liu, Y.; Long, D.; He, Q.; Singh, A. Effect of Cl- Accumulation on Corrosion Behavior of Steels in H_2S/CO_2 Methyldiethanolamine (MDEA) Gas Sweetening Aqueous Solution. *J. Nat. Gas. Sci. Eng.* **2016**, *30*, 444–454. [CrossRef]
44. Wang, S.; Zhang, G.; Fu, A.; Liu, Z.; Cao, X. The Corrosion and Tribological Behaviors of DLC Film in CO_2 Saturated NaCl Solution with High Cl^- Concentration. *Diam. Relat. Mater.* **2024**, *144*, 111016. [CrossRef]
45. *GB/T 20972.3-2025*; Petroleum and Natural Gas Industries—Materials for Use in H_2S-Containing Environments in Oil and Gas Production—Part 3: Cracking-Resistant CRAs (Corrosion-Resistant Alloys) and Other Alloys. Standards Press of China: Beijing, China, 2025.
46. *GB/T 19830-2023*; Petroleum and Natural Gas Industries—Steel Pipes for Use as Casing or Tubing for Wells. Standards Press of China: Beijing, China, 2023.
47. Ziomek-Moroz, M. Environmentally Assisted Cracking of Drill Pipes in Deep Drilling Oil and Natural Gas Wells. *J. Mater. Eng. Perform.* **2012**, *21*, 1061–1069. [CrossRef]
48. Liu, H.; Wang, B.; Ding, B.; Zheng, T.; Wen, C.; Zhang, H. Failure Behavior Analysis of the Main Shaft Threaded Joint of Ultra-Deep Top Drive Drilling Rig under Complex Loading Conditions. *Eng. Fail. Anal.* **2025**, *182*, 110090. [CrossRef]

49. Pilkey, W.D.; Pilkey, D.F.; Bi, Z. *Peterson's Stress Concentration Factors*; John Wiley & Son: Hoboken, NJ, USA, 2020.
50. Timoshenko, S.P.; Goodier, J.N. *Theory of Elasticity*, 3rd ed.; McGraw-Hill: New York, NY, USA, 1970.
51. MacDonald, K.A.; Deans, W.F. Stress analysis of drillstring threaded connections using the finite element method. *Eng. Fail. Anal.* **1995**, *2*, 1–30. [CrossRef]
52. Li, X.; Li, C.Y.; Qi, T.G.; Zhou, Q.S.; Liu, G.H.; Peng, Z.H. Reaction Behavior of Pyrite during Bayer Digestion at High Temperature. *Zhongguo Youse Jinshu Xuebao/Chin. J. Nonferrous Met.* **2013**, *23*, 829–835.
53. Ssemanobe, J.P.; Mutua, J.M.; Mose, B.R.; Olakanmi, E.O. Synergistic Effects of Chloride Ingress and Copper Deposition on Stress Corrosion Cracking in SA 210 Gr A1 Boiler Tubes. *Eng. Fail. Anal.* **2025**, *179*, 109761. [CrossRef]
54. Li, H.; Xu, H.; Li, Z.; Wang, X.; Song, F.; Zhou, Y.; Tang, J.; Gong, J. Degradation of 316 L Steel under Corrosion-Creep Interaction in Solar Salt: Effects of Stress Levels and Chloride Impurities. *J. Energy Storage* **2025**, *138*, 118492. [CrossRef]
55. Bulloch, J.H. Some Effects of Yield Strength on the Stress Corrosion Cracking Behaviour of Low Alloy Steels in Aqueous Environments at Ambient Temperatures. *Eng. Fail. Anal.* **2004**, *11*, 843–856. [CrossRef]

Disclaimer/Publisher's Note: The statements, opinions and data contained in all publications are solely those of the individual author(s) and contributor(s) and not of MDPI and/or the editor(s). MDPI and/or the editor(s) disclaim responsibility for any injury to people or property resulting from any ideas, methods, instructions or products referred to in the content.